









## Coupled valence carrier and core-exciton dynamics in WS<sub>2</sub> probed by few-femtosecond extreme ultraviolet transient absorption spectroscopy

Hung-Tzu Chang <sup>1,\*</sup>, Alexander Guggenmos <sup>1,†</sup>, Christopher T. Chen <sup>2</sup>, Juwon Oh <sup>1,‡</sup>, Romain Géneaux <sup>1,§</sup>, Yi-De Chuang <sup>3</sup>, Adam M. Schwartzberg <sup>2</sup>, Shaul Aloni <sup>2</sup>, Daniel M. Neumark <sup>1,4,¶</sup> and Stephen R. Leone <sup>1,4,5,\*\*</sup>

<sup>1</sup>*Department of Chemistry, University of California, Berkeley, California 94720, USA*

<sup>2</sup>*Molecular Foundry, Lawrence Berkeley National Laboratory, Berkeley, California 94720, USA*

<sup>3</sup>*Advanced Light Source, Lawrence Berkeley National Laboratory, Berkeley, California 94720, USA*

<sup>4</sup>*Chemical Sciences Division, Lawrence Berkeley National Laboratory, Berkeley, California 94720, USA*

<sup>5</sup>*Department of Physics, University of California, Berkeley, California 94720, USA*



(Received 16 March 2021; revised 28 July 2021; accepted 29 July 2021; published 23 August 2021)

Few-femtosecond extreme ultraviolet (XUV) transient absorption spectroscopy, performed with optical 500–1000-nm supercontinuum and broadband XUV pulses (30–50 eV), simultaneously probes dynamics of photoexcited carriers in WS<sub>2</sub> at the W O<sub>3</sub> edge (37–45 eV) and carrier-induced modifications of core-exciton absorption at the W N<sub>6,7</sub> edge (32–37 eV). Access to continuous core-to-conduction-band absorption features and discrete core-exciton transitions in the same XUV spectral region in a semiconductor provides a means to investigate the effect of carrier excitation on core-exciton dynamics. The core-level transient absorption spectra, measured with either pulse arriving first to explore both core-level and valence carrier dynamics, reveal that core-exciton transitions are strongly influenced by the photoexcited carriers. A  $1.2 \pm 0.3$  ps hole-phonon relaxation time and a  $3.1 \pm 0.4$  ps carrier recombination time are extracted from the XUV transient absorption spectra from the core-to-conduction-band transitions at the W O<sub>3</sub> edge. Global fitting of the transient absorption signal at the W N<sub>6,7</sub> edge yields  $\sim 10$  fs coherence lifetimes of core-exciton states and reveals that the photoexcited carriers, which alter the electronic screening and band filling, are the dominant contributor to the spectral modifications of core excitons and direct field-induced changes play a minor role. This work provides a first look at the modulations of core-exciton states by photoexcited carriers and advances our understanding of carrier dynamics in metal dichalcogenides.

DOI: [10.1103/PhysRevB.104.064309](https://doi.org/10.1103/PhysRevB.104.064309)

### I. INTRODUCTION

Studying the dynamics of elementary excitations in semiconductors such as photoexcited carriers, phonons, and excitons has been crucial to the success of electronic devices [1,2]. While most measurements on the photophysical and photochemical properties of semiconductors are performed within the optical domain, few-femtosecond to attosecond core-level transient absorption (TA) and transient reflectivity spectroscopy have recently been utilized to investigate carrier dynamics in semiconductors and two-dimensional materials [3–10] and the decay of core excitons in insulators [11–13]. Core-level TA spectroscopy in semiconductors typically consists of an optical pulse to excite the carriers in the sample

and an extreme ultraviolet (XUV) or x-ray pulse to record the changes in the core-level absorption spectra. In many semiconductors, the core-level absorption spectra can be mapped onto the conduction band (CB) density of states (DOS) due to significant dielectric screening [14], and the core-level TA spectra directly reflect the carrier distributions as a function of energy, thereby providing real-time tracking of carrier dynamics [4–7].

In contrast, the core-level absorption spectra of many insulators, in particular, ionic solids with poor dielectric screening, exhibit sharp peaks below the onset of core-to-CB edges [15]. These discrete transitions are termed “core excitons,” which are formed by the Coulomb attraction between the excited electron and the core hole [16,17]. The electron-hole binding results in longer lifetimes of the core excitons compared with the typical  $< 1$  fs decay time of core-to-CB transitions [18,19]. The observation of the decay of core excitons is enabled through attosecond transient absorption spectroscopy in the extreme ultraviolet, a core-level TA spectroscopy utilizing subfemtosecond XUV pulses in combination with  $< 5$ -fs-long optical pulses. As opposed to the typical XUV TA measurement in semiconductors where the XUV pulse probes the valence electronic state after optical excitation [3,4,7,8,20], those experiments probing core-exciton states use the sub-femtosecond XUV pulse to excite the core excitons, and

\*Present address: Department of Ultrafast Dynamics, Max Planck Institute for Biophysical Chemistry, 37077 Göttingen, Germany.

†Present address: UltraFast Innovations GmbH, Am Coulombwall 1, 85748 Garching, Germany.

‡Present address: Department of Chemistry, Soonchunhyang University, Asan 31538, Korea.

§Present address: Université Paris-Saclay, CEA, CNRS, LIDYL, 91191 Gif-sur-Yvette, France.

¶dneumark@berkeley.edu

\*\*srl@berkeley.edu

the core-exciton transition dipoles are subsequently perturbed with the optical pulse [11–13], analogous to the studies on the decay of atomic Rydberg states and autoionization states [21]. Due to the large band gap in insulators, which exceeds the photon energy of available visible and ultraviolet light pulses, the observation of the effect of carrier dynamics on a core-excitonic system via core-level TA spectroscopy has not been achieved, and the effect of valence electron-hole pairs on core-exciton transitions and their dynamics remains elusive.

In this paper, we report the observation of core-exciton transitions within the W  $N_{6,7}$  edge (32–37 eV) of  $WS_2$  and a smooth core-level absorption edge at the nearby W  $O_3$  transition (37–45 eV), which consists of core-to-CB transitions that can be understood within the single-particle mean-field picture. The proximity of the two different types of core-level absorption edges presents an excellent opportunity in simultaneously observing the dynamics of carriers in the valence shell and their influence on the dynamics of core excitons. A single experiment thus probes the carriers at the W  $O_3$  edge and the discrete core-exciton transitions at the W  $N_{6,7}$  edge. Tungsten disulfide is a group VI transition metal dichalcogenide and a semiconducting two-dimensional (2D) layered material. In its mono- and bilayer form, the electronic structure and photophysics of  $WS_2$  have been extensively studied for potential applications in optoelectronics and 2D valleytronics and spintronics [22–34]. Recently, interlayer charge-transfer excitations and novel elementary excitations such as moiré excitons were observed in heterostructures containing  $WS_2$  layers [35–38].

Here, by conducting core-level transient absorption spectroscopy in the XUV on  $WS_2$  thin films, picosecond hole relaxation and carrier recombination times are obtained from the core-level TA spectra at the W  $O_3$  edge. An  $\sim 10$  fs coherence lifetime of core excitons at the W  $N_{6,7}$  edge is also measured. In contrast to the attosecond XUV TA studies on insulators, where the observed dynamics are dominated by coupling of core-exciton states with the optical field [11–13], here the core-exciton lineshape is primarily influenced by the change in electronic screening and band filling due to carriers excited by the optical pulse. This optical-XUV transient absorption study at the W  $O_3$  and  $N_{6,7}$  edges provides a prototypical example for measuring the carrier-induced modification of core excitons and paves the way for exploring carrier dynamics in 2D heterostructures and superlattices involving transition metal dichalcogenides, where the element specificity of core-level TA spectroscopy can be employed to enable layer-selective probing of photophysical and photochemical phenomena.

## II. EXPERIMENTAL SCHEME

The details of sample preparation and the scheme of the XUV TA spectroscopy experiment are provided in Appendices A and B, respectively. In brief, 40-nm-thick  $WS_2$  films were synthesized on 30-nm-thick silicon nitride windows by atomic layer deposition (ALD) of  $WO_3$  thin films and subsequent sulfurization with  $H_2S$  [39]. In the XUV TA experiments, the samples were irradiated with a broadband optical pulse (500–1000 nm) with nominal duration of 4 fs and a time-delayed broadband XUV pulse (30–50 eV) produced

by high-harmonic generation using a near-single-cycle optical pulse in a Kr gas jet.

## III. RESULTS AND DISCUSSION

The core-level absorption spectrum of the 40-nm-thick  $WS_2$  film is displayed in Fig. 1(a) (red line). The static spectrum below 37 eV (marked with the dashed cyan line) exhibits four distinct peaks labeled as A–D. Peaks A and B occur on top of the absorption edges between 33 and 34 eV. Peak C exhibits a Fano-type asymmetric lineshape at approximately 35.5 eV with fine-structure peak D occurring at approximately 36.6 eV [40]. A smooth absorption feature extends from 38.5 eV to beyond 45 eV. By comparing the measured spectrum with the calculated imaginary part of the dielectric function using the all-electron full-potential linearized augmented plane wave (FP-LAPW) method (Appendix C) with random phase approximation [41,42], the smooth absorption feature above 38.5 eV is assigned to the transition between the W  $5p_{3/2}$  core bands and the CB (W  $O_3$  edge). Peaks A and B are assigned to the W  $4f_{7/2}$  transitions (W  $N_7$  edge), and peaks C and D are assigned to the transitions from W  $4f_{5/2}$  core levels to the CB (W  $N_6$  edge). The comparison between the measured W  $5p_{3/2}$  absorption edge and the calculated dielectric function [Fig. 1(a), dashed black line] indicates significant lifetime broadening of the W  $5p_{3/2}$ -to-CB transitions. In addition, the peaks measured at the absorption edges between 32 and 37 eV are clearly different from the smooth onset of the  $4f$ -to-CB transitions [Fig. 1(a), dash-dotted black line] calculated with mean-field approximation, suggesting that many-body interactions between the electron and the core hole contribute to the measured discrete lineshape. Note that the broadband XUV pulse (30–50 eV) covers the core-level transitions from both the W  $4f$  and  $5p$  orbitals, enabling simultaneous observation of dynamics at the two different edges.

Typical core-level TA spectra between  $-40$  fs and 2.6 ps time delay are displayed in Fig. 1(b). In this paper, the time delay is defined as the arrival time of the XUV pulse subtracted from the time of the optical pulse, and positive time delay indicates that the samples are probed by the XUV pulse “after” optical excitation. The change in absorbance  $\Delta A(t)$  at a specific time delay  $t$  is defined as  $\Delta A(t) = A(t) - A(t = -40 \text{ fs})$  with  $A$  denoting absorbance. The pump-excited carrier density is estimated to be  $1 \times 10^{21} \text{ cm}^{-3}$  or  $6 \times 10^{13} \text{ cm}^{-2}$  per layer (Appendix D). Between 37 and 40 eV below the W  $O_3$  edge, two weak, broad positive features are observed [Fig. 1(b)]. Although the difference in static absorbance below and above the W  $N_{6,7}$  edge, or “edge jump,” is much smaller than the W  $O_3$  edge [Fig. 1(a)], the XUV TA signal occurring near transitions A, B, and C is narrow and much stronger than the TA signal above 37 eV [Fig. 1(b)]. Clearly, the natures of the W  $N_{6,7}$  edge transitions (peaks A–D) and the W  $O_3$  edge transitions are different, and separate treatment is needed to understand their corresponding XUV TA spectra.

When a core electron is excited into the CB, the excited electron can interact with the core hole via Coulomb attraction. In many semiconductors, the electronic screening reduces the Coulomb interaction such that the core-level transitions can still be understood in a single-particle picture [14].

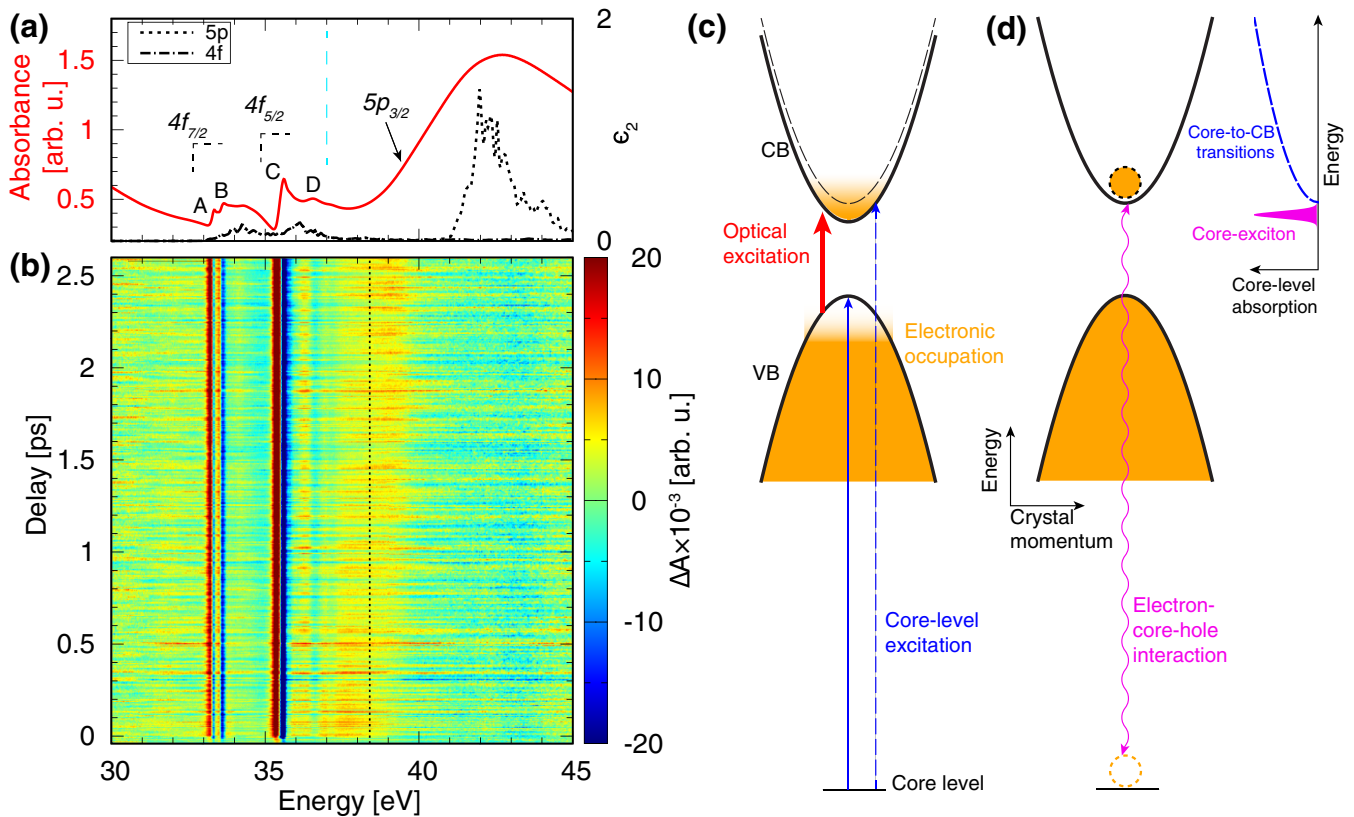


FIG. 1. (a) Static core-level absorption spectrum of a 40-nm-thick  $\text{WS}_2$  film (red line). The dashed and dash-dotted black lines show the computed imaginary part of the dielectric function  $\epsilon_2(\omega)$  from the  $5p$  and  $4f$  core bands, respectively. (b) exhibits the XUV TA spectra between  $-40$  fs and  $2.6$  ps delay. To serve as a reference (see text), a dashed cyan line is plotted at  $37$  eV in (a), and a dashed black line is plotted at  $38.4$  eV in (b). The scheme for a typical core-level TA measurement in highly screened semiconductors is shown in (c), where the core-level excitation probes the electronic occupation in the VB and CB plus the energy shift of the bands. (d) illustrates the formation of the core exciton through electron–core-hole attraction and its corresponding absorption spectrum.

As the core bands are dispersionless, the core-level transitions map the CB density of states and, with optically excited carriers in the valence band (VB) and CB, core-level transitions probe the electronic occupation in the valence shell and the energy shifts of the VB and CB due to carrier and phonon excitations [Fig. 1(c)] [4–7]. This scheme corresponds to the smooth  $\text{W O}_3$  edge transitions above  $37$  eV but cannot describe the transitions at the  $\text{W N}_{6,7}$  edge.

Discrete peaks form in core-level absorption spectra when the Coulomb attraction between the electron and the core hole is non-negligible. The interaction between the core hole and the electron excited by the XUV or the x-ray renormalizes the core-level absorption, and discrete “core-exciton” peaks can form near the critical points of the core-to-CB transitions [Fig. 1(d)] [16]. Note that excitonic interactions between the excited electron and the core hole are present for all core-to-CB absorptions. Therefore the renormalization of the core-level absorption spectra is not limited to the near-edge transitions, but may extend several eV above the edge [43,44]. The behavior of transitions at the  $\text{W N}_{6,7}$  edge below  $37$  eV is consistent with the description of core excitons. To verify this, we compare the XUV TA spectra of the  $\text{W N}_{6,7}$  and  $\text{W O}_3$  edges near zero time delay.

Figure 2(a) displays the XUV TA spectra between  $-25$  and  $+25$  fs time delay; lineouts of the XUV TA spectra at

five different time delays between  $-20$  and  $+7$  fs are plotted in Fig. 2(b). At positive delays, the XUV light probes the changes due to photoexcitations in the valence shell, while at negative time delays, the optical pulse perturbs the core-level transition dipole before its decay by both carrier photoexcitation and the direct coupling of the core-excitonic transitions with the optical field [11–13]. The distinction between the transitions at the  $\text{W N}_{6,7}$  edge and the  $\text{W O}_3$  edge can be visualized in the XUV TA signal at negative delays. While the TA signal at the  $\text{W O}_3$  edge ( $37$ – $40$  eV) diminishes to zero at less than  $-4$  fs time delays, TA signals near peaks A, B, and C are still visible at less than or equal to  $-10$  fs time delays. The experimental results thus indicate that transitions A, B, and C are more long-lived than the transitions below the  $\text{W O}_3$  edge. The comparison of core-level transition lifetimes corroborates the assignment that the peaks within the  $\text{W N}_{6,7}$  edge [Fig. 1(a)] are core excitons because the electron–core-hole attraction of the core exciton stabilizes the core-excited state and enables a longer lifetime [18]. The broad positive feature above  $37$  eV at positive time delays can then be interpreted as photoexcited holes in the VB. In the following, we first focus on the measured dynamics induced by photoexcited carriers at the  $\text{W O}_3$  edge. Next, we discuss the measured TA spectra of core-exciton transitions at the  $\text{W N}_{6,7}$  edge at both positive and negative time delays.

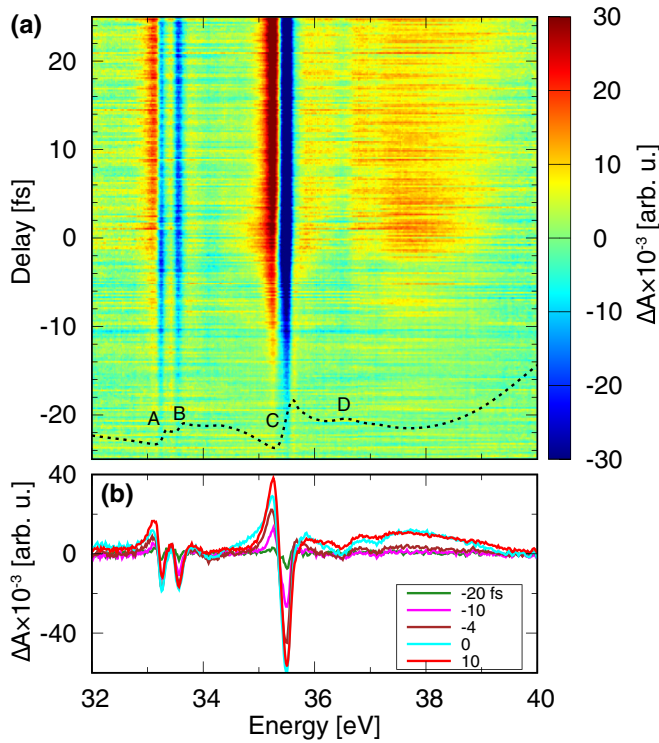


FIG. 2. (a) XUV TA signal between  $-25$  and  $+25$  fs time delay. The static spectrum is plotted as a dashed black line as a reference. (b) shows the XUV TA lineouts at five different time delays between  $-20$  and  $10$  fs.

### A. Carrier dynamics at the $W O_3$ edge

To understand the XUV TA signal at the  $W O_3$  edge, XUV TA spectra at five different time delays between  $+7$  fs and  $+2$  ps are presented in Fig. 3(a). At energies above the edge ( $41$ – $45$  eV), the XUV TA spectra exhibit a weak decrease in absorbance (negative  $\Delta A$ ) throughout the entire range of delays, whereas two positive features with different dynamical behavior are observed between  $37$  and  $40$  eV below the edge. The feature spanning  $37$ – $38.4$  eV decays with time, while the feature between  $38.4$  and  $39.5$  eV, which is barely observable near time zero, increases in magnitude with the time delay.

The positive and negative  $\Delta A$  below and above the edge might initially suggest that the positive feature is due to holes in the VB, which open up new excitation pathways from the core, and the negative feature is due to electrons in the CB, which blocks the core-level excitations into the CB. The different dynamical behaviors between  $37$ – $38.4$  eV and  $38.4$ – $39.5$  eV could then be assigned to relaxation of the photoexcited hot hole to the VB edge. However, such an assignment implies that the transition from the core to the VB edge is at approximately  $39.5$  eV and the initially photoexcited holes are located approximately  $2$  eV below the VB maximum. Given the approximately  $2$  eV direct band gap of bulk  $WS_2$  [22], this suggests an optical transition energy of approximately  $4$  eV, far exceeding the maximum photon energy at  $2.5$  eV of the optical pulse. Therefore the positive feature between  $38.4$  and  $39.5$  eV cannot be assigned to holes in the VB. Instead, it can be interpreted as a redshift of the  $W O_3$  edge due to band gap renormalization. Both the change in

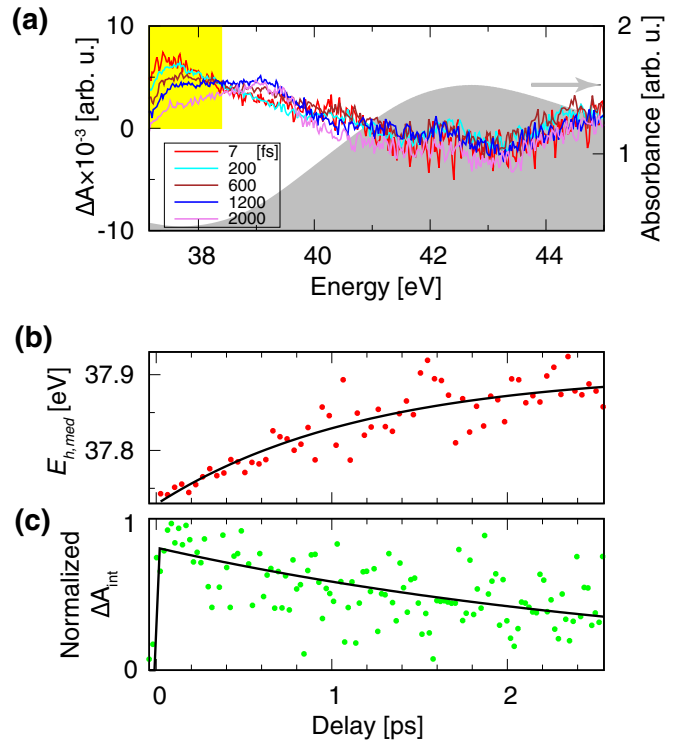


FIG. 3. (a) XUV TA spectra at the  $W O_3$  edge at five different time delays. The static core-level absorption spectrum is plotted in gray as a reference. (b) shows the median energy  $E_{h,med}$  of the TA signal between  $37.4$  and  $38.4$  eV [yellow shaded area in (a)], and (c) shows the integrated XUV TA signal in the same energy region.

electronic screening and phonon heating due to photoexcited electrons and holes can lead to band gap renormalization, resulting in the lowering of the CB edge and therefore a redshift of the core-to-CB transition energies [4]. As energy dissipates from the electronic domain, the increase in phonon temperature and the heat-induced lattice expansion can further enhance band gap renormalization and lowering of the CB [45], which causes the positive features to grow with time delay. In addition, with the assignment of the positive feature spanning  $38.4$ – $39.5$  eV as due to the phonon-induced edge shift, the feature between  $37$  and  $38.4$  eV, which diminishes with increasing time delay, can then be assigned to holes.

To track the hole relaxation process, the median energy of the hole signal  $E_{h,med} = \frac{\int E \Delta A dE}{\int \Delta A dE}$  is plotted in Fig. 3(b). The median energy  $E_{h,med}(t)$  shifts from  $37.7$  to  $37.9$  eV with respect to time and can be fitted by a single exponential with a time constant of  $1.2 \pm 0.3$  ps. In addition, as holes relax to the VB edge at the long-time limit, the core-to-VB edge transition energy can be determined from  $E_{h,med}(t \rightarrow \infty)$ . The extracted transition energy from the core to the VB edge from the exponential fitting is  $37.9$  eV. The proximity between the hole feature and the positive feature due to band gap renormalization leads us to assign the core-to-VB edge transition with the median energy of the hole feature at the long-time limit rather than use the maximum energy cutoff of the hole feature as in the core-level TA studies of germanium and  $2H-MoTe_2$  [4,7].

Consulting the band structure diagram of  $WS_2$  [Fig. 4(b)] and the initial photoexcited carrier distribution that is

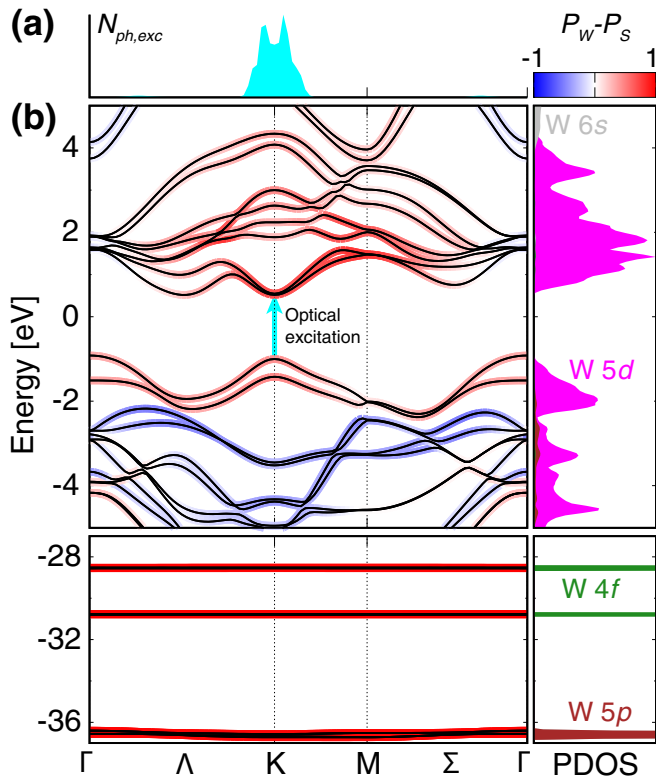


FIG. 4. (a) Number of photons in the optical pulse available to excite carriers from the VB to the CB as a function of  $k$  points (Appendix C). (b) shows the band structure and projected density of states (PDOS) of  $\text{WS}_2$  calculated with the FP-LAPW method (Appendix C). The colors on the bands (left panel) reflect the difference between the atomic orbital projection on W and S ( $P_W - P_S$ ).  $P_n$  is the sum of the modulus square of the wave-function projections of atom  $n$ .

proportional to the number of photons available for excitation as a function of crystal momentum [Fig. 4(a)], the initial carrier distribution is characterized as residing mainly within the  $K$  valley, and the carriers in the  $\Gamma$  valley near the VB maximum are barely excited. The results suggest that the 1.2 ps timescale of hole relaxation is related to the intervalley redistribution of holes between the  $K$  valley and the  $\Gamma$  valley (VB maximum) mediated by hole-phonon interactions.

In addition, Fig. 4(b) shows that the orbital character near the top of the VB and the bottom of the CB is dominated by W 5d orbitals, indicating that the core-level transitions from W 4f and 5p states are both sensitive to carrier dynamics near the band edges. This excludes the possibility that the diminishing TA signal ranging from 37 to 38.4 eV is due to carriers reaching band regions where core-level transitions from W 4f and 5p orbitals are forbidden. The loss of holes in the VB due to recombination is characterized by the integrated TA signal  $\Delta A_{\text{int}} = \int \Delta A dE$  over the 37–38.4 eV range [Fig. 3(c)]. The magnitude of  $\Delta A_{\text{int}}$  as a function of time can be fitted by a single exponential with a decay constant of  $3.1 \pm 0.4$  ps convoluted by the instrument response function. The 3.1 ps decay is therefore assigned to the carrier recombination time as the hole signal (37–38.4 eV) decays to zero at the long-time limit.

The assignment of the VB maximum at 37.9 eV suggests that a negative TA feature due to excited electrons is expected at 39.9 eV ( $37.9 + 2$  eV band gap). While a weak negative TA signal barely above the noise level is indeed observed spanning 41–45 eV, assigning this to the CB electrons plus the VB maximum at 37.9 eV would suggest an electron-hole energy separation of at least 3 eV, which exceeds the maximum photon energy of 2.5 eV in the optical pulse. In addition, no significant dynamics are observed for the negative feature between 41 and 45 eV, whereas the electrons are expected to recombine with the holes within the observed 3.1 ps recombination time. This indicates that the weak signal at  $\geq 41$  eV may be caused by changes in core-hole lifetime, which affects the spectral broadening of the edge, or a decrease in oscillator strength of the W  $\text{O}_3$  edge due to carrier and phonon excitations [7,46], rather than directly due to the photoexcited electrons in the CB.

The absence of the XUV TA signal due to occupation of photoexcited electrons in the CB can be explained by the significant spectral broadening above the W  $\text{O}_3$  edge, where the experimentally measured static spectrum is much wider and smoother than the calculated dielectric function according to the projected CB DOS [Fig. 1(a)]. Here, the fine structure in the projected CB DOS due to critical points in the CB is completely lost in the measured absorption edge. This is in contrast to the recently studied  $L_{2,3}$  edge in Si and Te  $\text{N}_{4,5}$  edge in 2H-MoTe<sub>2</sub> where the critical points in the CB can be directly mapped onto the core-level absorption spectrum [7,47]. The broadening in the W  $\text{O}_3$  edge increases the overlap between the expected negative XUV TA feature due to electron occupation in the CB and the positive feature due to CB redshift. The overlapping negative and positive features thus lead to the cancellation between the two and make extracting the electron distribution in the CB from core-level TA spectra here unreliable.

## B. Dynamics and lifetimes of core excitons at the W $\text{N}_{6,7}$ edge

While the core-level TA spectra at the W  $\text{O}_3$  edge can be explained by the redshift of CB and electronic occupation in the VB and CB, XUV TA signals of core-exciton transitions within the W  $\text{N}_{6,7}$  edge cannot be interpreted with the same approach. Note that unlike the insulators where core-exciton dynamics have only been observed when XUV light arrives first [11–13], here the XUV TA signal at the core-exciton transitions extends throughout the entire range of positive time delays [Figs. 1(b) and 2(a)]. This difference arises because in insulators, the band gap exceeds the photon energy range of the optical pulse, so electron-hole pairs in the VB and CB are not excited. Thus the core excitons can only be perturbed by optical-field-induced coupling of core-exciton states. Here, photoexcited carriers with picosecond lifetimes can instantaneously “dress” the XUV-excited core excitons by the carrier-induced change in band filling and electronic screening [48,49]. Therefore carrier-induced modification of the core-exciton lineshape occurs at both negative and positive time delays.

In Fig. 2(a), the core-level TA signal at short ( $< 25$  fs) positive delays is solely due to photoexcited carriers since dynamics caused by electron-phonon scattering occur on a

timescale of  $10^2$  fs and can be ignored [50–52]. While photoexcited carriers are the sole contributor to the modification of core excitons at short positive time delays, at negative delays direct field-induced changes can also modify the core-exciton lineshape. It has been shown that similar to atomic autoionizing states [21,53–56], the optical pulse can cause energy shifts of the core-exciton transitions through the AC Stark effect and resonant coupling between the core-exciton states or with the ionization continuum [11–13]. Formal treatment of the XUV TA spectra at negative time delays requires computation of the free induction decay of the core-exciton transition dipoles by solving a time-dependent Schrödinger equation, including couplings of the core-level transitions with both the photoexcited carriers and the optical field [11–13,54]. However, due to the complexity in including the many-body interactions between the core-level transitions and the photoexcited carriers, which is detailed in the next section, we propose an alternative method to separate the contribution from photoexcited carriers and the optical field by their different time behaviors.

Here, we analyze the different contributions by applying global fitting to the XUV TA spectra  $\Delta A$  through singular value decomposition (SVD) (Appendix E):  $\Delta A(t, E) = \sum_n s_n u_n(t) v_n(E)$ . Functions  $\{u_n(t)\}$  and  $\{v_n(E)\}$  are singular vectors, or *components*, ranked by singular values  $\{s_n\}$  in descending order. Transition D is excluded from the analysis due to poor signal in that spectral region. The XUV TA signal from the largest component at transitions A and B is shown in Fig. 5(a), showing good agreement with experimental data [Fig. 2(a)] and indicating that the dynamics at transitions A and B can be described by a single component. The corresponding singular vector [Fig. 5(b)] directly reflects the TA signal measured at +10 fs time delay [Fig. 2(b)], and the dynamics of the component [Fig. 5(c)] exhibits an exponential decay at negative delay and becomes constant when  $t > 0$ . This indicates that transitions A and B have similar decay dynamics and lifetimes, and although the optical pulse can potentially affect the core excitons directly through coupling the core-exciton transition dipoles with the optical field, the carriers excited in the valence shell remain the dominant influence on core excitons A and B.

Within their decay time, core excitons A and B are modulated by the valence electron-hole pairs. By fitting the decay dynamics with a single exponential [Fig. 5(c)], a core-exciton coherence lifetime ( $T_2$ ) of  $10.9 \pm 0.4$  fs is extracted. The decoherence in core-exciton transitions can be caused by population decay through Auger processes or by exciton-phonon coupling [11–13]. Previous studies on the decay of core excitons in insulators show that when exciton-phonon coupling prevails over other decoherence channels, the free induction decay of the core-exciton transition dipole moment exhibits a Gaussian decay [11–13] that leads to a Gaussian spectral profile [57,58]. Here, the decay of XUV TA signal at negative time delays is exponential rather than Gaussian [Figs. 5(c) and 5(f); a comparison between Gaussian and exponential fitting is detailed in Appendix E], suggesting that phonon-induced dephasing is insignificant and Auger processes are the dominant contributor to core-exciton decay. Thus a population decay time ( $T_1 \approx T_2/2$ ) at  $5.5 \pm 0.2$  fs can be inferred [59].

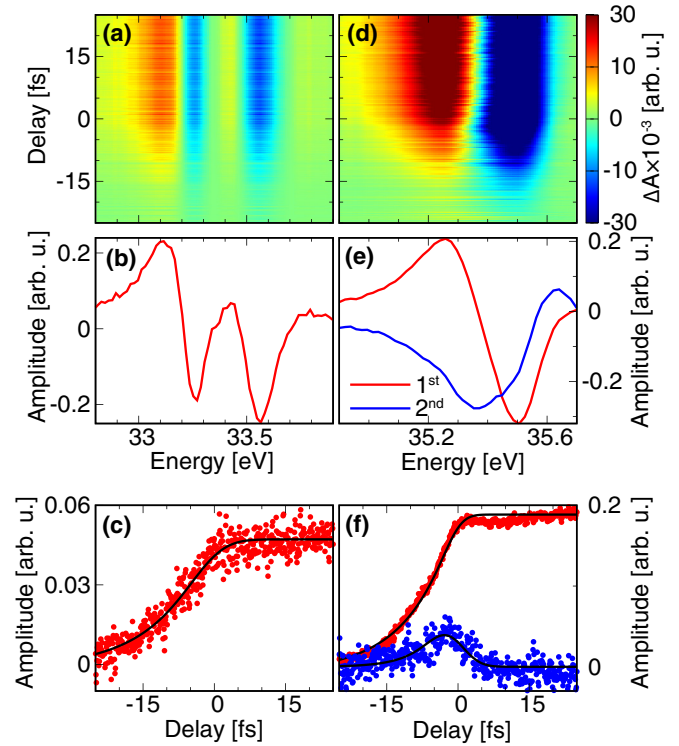


FIG. 5. (a) XUV TA signal from the largest component in SVD for transitions A and B; the corresponding singular vector with respect to energy and time is shown in (b) and (c), respectively. (d) exhibits the XUV TA signal from the two highest ranked components in SVD for transition C; the corresponding singular vectors for the first and second largest singular values as a function of energy and time are shown in (e) and (f), respectively. The XUV TA signal from only the largest component in SVD for transition C is shown in Fig. 10 (Appendix E). Note that the magnitude of the singular value of each component is included in the amplitude shown in (c) and (f).

To quantitatively reproduce the XUV TA spectra at transition C [Fig. 2(a)], the two largest components in the SVD are required [Fig. 5(d)]. The dynamics of the two components [Fig. 5(f)] show that at  $>10$  fs delays, the largest (first) component is constant whereas the second component is zero. In addition, the second component only becomes nonzero either at negative time delays or during pulse overlap. This indicates that the largest component represents the influence of carriers on the core exciton and the second component originates from the direct coupling of the core exciton to the optical field, because in contrast to the direct coupling to the optical field that can only occur when the field overlaps with the transition dipole before its decay, the carriers are much longer lived than the transient optical pulse and can cause spectral changes at  $>10$  fs time delays. The field-induced TA component [Fig. 5(e), blue line] exhibits a negative amplitude below the edge and a positive amplitude above [cf. Fig. 6(b)]. The asymmetry of the XUV TA amplitude centered around the edge suggests that it may relate to the change in the Fano  $q$  factor of the transition, which can be induced by the optical pulse through a ponderomotive phase shift [54], or direct coupling to neighboring core-excited states [55]. Fitting the

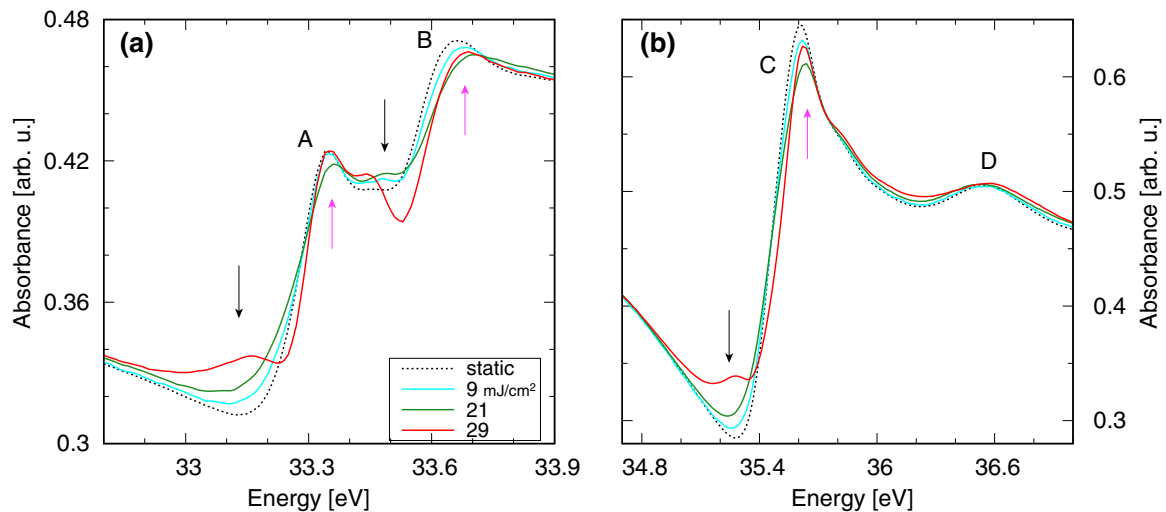


FIG. 6. Fluence dependence measurement of core-level absorption spectra at transitions (a) A and B and (b) C and D, at +10 fs time delay. The static spectrum is shown as a black dashed line as a reference. The estimated excited carrier density (Appendix D) at pump fluences 9, 21, and 29 mJ/cm<sup>2</sup> is  $4.5 \times 10^{20}$ ,  $1.0 \times 10^{21}$ , and  $1.5 \times 10^{21}$  cm<sup>-3</sup>, respectively.

dynamics of the largest component with a single exponential yields a core-exciton coherence lifetime of  $9.6 \pm 0.1$  fs.

### C. Carrier-induced modification of core-exciton transitions within the W N<sub>6,7</sub> edge

In this section, we focus on the modification of the core-exciton absorption lineshape by photoexcited carriers. First, we compare the effect of photoexcited carriers on core-exciton and core-to-band absorption at +10 fs time delay [Fig. 2(b)]. In contrast to the broad, positive TA signal observed below the W O<sub>3</sub> edge, no positive signal is observed between 30 and 33 eV [Fig. 1(b)], and the majority of the TA signal occurs near core-exciton transitions A–C. The lack of XUV TA signal directly from the electronic state blocking of carriers as at the W O<sub>3</sub> edge can be attributed to the renormalization of core-level absorption spectra due to core-exciton formation. The formation of core excitons concentrates the oscillator strength of core-to-CB transitions to the bound core-excitonic states, and the core-level absorption spectra no longer map to the CB DOS. In addition, the oscillator strength at the W N<sub>6,7</sub> edge is lower than the W O<sub>3</sub> edge. Compared with the edge change (jump) of 1 optical density (OD) below and above the W O<sub>3</sub> edge, the W N<sub>6,7</sub> edge has an edge jump of  $\leq 0.5$  OD [Fig. 1(a)]. This indicates that the signal of electronic state blocking, if present at the W N<sub>6,7</sub> edge, would be much lower than the signal below the W O<sub>3</sub> edge (37.4–38.4 eV), which is already close to the noise level.

To understand the effect of carriers on core-exciton transitions, the core-level absorption spectra at +10 fs time delay with three different optical pump fluences are displayed in Fig. 6. While transition D is broadened with increasing pump fluence, the carrier-induced changes at A, B, and C are much more complex. At transitions A, B, and C, the absorption edge shifts to higher energy with increasing pump fluence. However, the changes in absorbance below and above the edge are nonmonotonic with increasing optical excitation. At fluences between 0 and 21 mJ/cm<sup>2</sup>, the absorbance below the edges

(Fig. 6, black arrows) increases while the absorbance above the edge (Fig. 6, magenta arrows) decreases with increasing fluence. At a fluence of 29 mJ/cm<sup>2</sup>, the absorbance above the edge increases rather than decreases compared with the absorbance at 21 mJ/cm<sup>2</sup> pump fluence. In addition, shoulders and ripples start appearing around transitions A, B, and C at a fluence of 29 mJ/cm<sup>2</sup>. New small features appear below the edge of A and C, and a dip appears below absorption edge B. Clearly, the carrier-induced changes to the core-exciton transitions cannot be simply described by an energy shift or a broadening of the lineshape.

The behavior of the core-exciton spectral change at +10 fs delay with respect to increasing pump fluence is reminiscent of the changes in optical absorption of valence excitons in highly excited semiconductors [49]. For example, it has been observed that in highly excited GaAs, the absorption peak of bound excitons decreases in magnitude and new features below the onset of excitons appear in the optical absorption spectra [48]. Using a generalized Elliott formula [60–62], Lee *et al.* showed that the contributions to the optical absorption spectra of highly excited semiconductors can be divided into three categories [48]. First, the ionization of bound excitons due to the screening of the photoexcited electron-hole plasma causes suppression of the bound exciton transitions and an overall blueshift of the absorption edge. Second, the increasing band filling causes ripples to appear around the exciton transitions, especially below the absorption onset. Third, the carrier-induced band gap renormalization introduces a redshift of the CB edge that partially compensates the blueshift of absorption onset due to suppression of bound exciton transitions.

The phenomena observed for optical excitons can analogously explain the spectral changes in core-exciton transitions here. The increase in electronic screening due to electron-hole excitations in the VB and CB suppresses bound core-exciton transitions and contributes to the overall blueshift of the absorption onset. The changes in band filling in the valence shell modulate the core-excited states' energies, oscillator

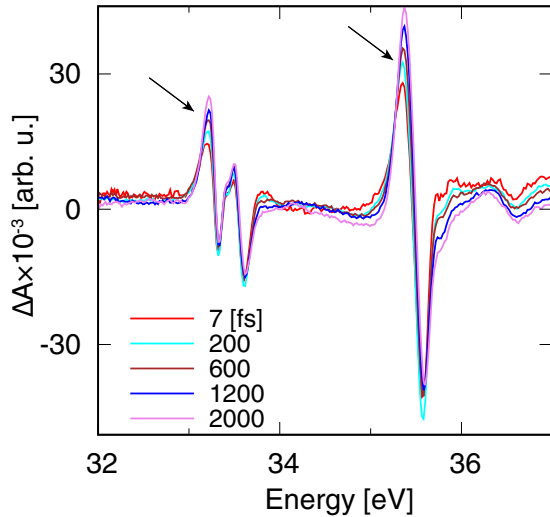


FIG. 7. XUV TA spectra at five different positive time delays between 0 and 2 ps.

strengths, and coupling to the continuum, so that new absorption features appear.

The similar behavior between the carrier-dressed core-exciton lineshape and optical absorption in highly excited semiconductors, which can be simulated analytically, leads us to explore the possibility of extending the formalism [61] to quantitatively extract parameters such as core-exciton radii and binding energies. The generalized Elliott formula [60–62] is based on a parabolic two-band model that only incorporates a single CB minimum. As core-exciton features B and D are clearly embedded in the core-to-CB continuum transitions, the parabolic two-band approximation is no longer applicable. In addition, due to the dispersionless core bands, core excitons can form at multiple CB minima, e.g., at the  $K$ ,  $\Lambda$ , and  $\Sigma$  valleys (Fig. 4), and the wave functions at those CB minima can further hybridize. Therefore quantitative treatment of the core-exciton transitions here, and by extension, their modification due to carriers, will require Bethe-Salpeter equation calculations including the full band structure of  $\text{WS}_2$  [63–65], which is beyond the scope of this work.

#### D. Picosecond XUV transient absorption signal at the $\text{W N}_{6,7}$ edge

As photoexcited carriers are the major contributor to the modulations of the core-exciton spectra at negative and short positive time delays, we consider here the possibility of using the TA spectra of core excitons to extract carrier dynamics. Although picosecond carrier relaxation and recombination would suggest a decay of TA signal at the core-exciton transitions, a growth of TA signal (Fig. 7, black arrows) is observed below transitions A and C with increasing time delay, and no significant TA change is measured above the edge at transitions A, B, and C throughout 0–2.6 ps. This indicates that in addition to photoexcited carriers, the excitation of phonons through electron-phonon interactions also contribute to the spectral changes in core excitons at long time delays, as phonon-induced band gap renormalization can induce a redshift of CB that is consistent with the positive TA signal

observed below the transitions. Therefore the core-exciton transitions at the  $\text{W N}_{6,7}$  edge here are poorly configured for extraction of carrier dynamics, because the spectral changes due to carriers and phonons at hundreds-of-femtoseconds to picosecond timescales cannot be easily separated.

#### E. Comparison between the core-exciton and core-to-conduction-band transitions

The contrasting behavior of core-exciton transitions at the  $\text{W N}_{6,7}$  edge and the core-to-band transitions at the  $\text{W O}_3$  edge in the same energy range is highly unique and suggests that factors other than the macroscopic screening, which are experienced by transitions from both  $\text{W } 4f$  and  $5p$  core levels, are contributing to the core-exciton formation. As the CB minima are dominated by  $\text{W } 5d$  orbitals that are accessible from both  $\text{W } 4f$  and  $5p$  through XUV photons, it is thus suggested that the contributor to the difference between the  $\text{W N}_{6,7}$  edge and the  $\text{W O}_3$  edge absorption lies in the properties of the core orbitals. The  $\text{W } 4f$  orbitals involved at the  $\text{W N}_{6,7}$  edge are far more localized than the  $\text{W } 5p$  orbitals for the  $\text{O}_3$  edge transitions. The localized core hole may then act as a point positive charge and modulate the electronic wave functions in the CB to form a core exciton [17].

## IV. CONCLUSION

In summary, photoinduced dynamics at  $\text{W N}_{6,7}$  and  $\text{O}_3$  edges in  $\text{WS}_2$  are simultaneously measured by XUV core-level transient absorption spectroscopy. Picosecond hole relaxation and recombination dynamics in the valence band are extracted from the transient absorption spectra of the core-to-conduction-band transitions at the  $\text{W O}_3$  edge. Lifetimes of core-excited states at the  $\text{W O}_3$  edge and the  $\text{W N}_{6,7}$  edge are obtained from XUV transient absorption spectra at negative time delays. While the lifetimes of  $\text{W O}_3$  edge transitions are well below the duration of the optical pulse ( $\sim 4$  fs), core-exciton coherence lifetimes up to 11 fs are observed at the  $\text{W N}_{6,7}$  edge. Global fitting of the XUV transient absorption spectra at short time delays reveals that in contrast to the direct field-induced core-exciton dynamics observed in insulators [11–13], carrier-induced modulation of core-exciton states dominates the dynamics at the few-tens-of-femtoseconds timescale.

The drastically different behaviors between the absorption from the  $\text{W } 5p$  and  $4f$  core orbitals in the same energy region suggest that in addition to macroscopic screening, the degree of localization of the core orbitals can contribute significantly to the core-level absorption lineshape and the formation of core excitons. The observation of carrier-modulated core-exciton transitions can serve as an initial step in further understanding and manipulating the dynamics of core excitons in condensed matter, and the extraction of hole dynamics at the  $\text{W O}_3$  edge further advances the use of core-level TA spectroscopy in measuring carrier dynamics in transition metal dichalcogenides and their heterostructures.

## ACKNOWLEDGMENTS

The authors would like to thank V. C. Tung, X. Wei, F. de Groot, D. Y. Qiu, F. H. da Jornada, H. Wang, and



D. Prendergast for fruitful discussions. The authors would also like to thank T. Kuykendall for help during sample synthesis. Investigations were supported by Defense Advanced Research Projects Agency PULSE Program Grant No. W31P4Q-13-1-0017 (concluded), U.S. Air Force Office of Scientific Research Grants No. FA9550-19-1-0314, No. FA9550-20-1-0334, No. FA9550-15-0037 (concluded), and No. FA9550-14-1-0154 (concluded), Army Research Office Grant No. W911NF-14-1-0383, and W. M. Keck Foundation Award No. 046300-002. This research used resources of the Molecular Foundry and the Advanced Light Source, U.S. DOE Office of Science User Facilities, under Contract No. DE-AC02-05CH11231. Core-level absorption simulations were conducted at Molecular Graphics and Computation Facility, UC Berkeley College of Chemistry, funded by National Institute of Health (NIH Grant No. S10OD023532). H.-T.C. acknowledges support from Air Force Office of Scientific Research (AFOSR) (Grants No. FA9550-15-1-0037 and No. FA9550-19-1-0314) and the W. M. Keck Foundation (Grant No. 046300-002); A.G. acknowledges support from the German Research Foundation (Grant No. GU 1642/1-1); J.O. is supported by the W. M. Keck Foundation (Grant No. 046300-002) and Basic Science Research Program through the National Research Foundation of Korea funded by the Ministry of Education (Grant No. 2019R1A6A3A03032979). D.M.N. acknowledges support from the U.S. Air Force Office of Scientific Research (Grant No. FA9550-15-0037, concluded) and the Army Research Office under Grant No. W911NF-20-1-0127.

#### APPENDIX A: SAMPLE PREPARATION

The  $\text{WS}_2$  sample was synthesized by atomic layer deposition of  $\text{WO}_3$  thin films on 30-nm-thick silicon nitride membranes (Norcada Inc.). The tungsten oxide film was subsequently converted into sulfide in a tube furnace with  $\text{H}_2\text{S}$ . Before atomic layer deposition, 16-nm-thick silicon nitride films were deposited onto the Si frame of the silicon nitride windows using plasma-enhanced chemical vapor deposition (PECVD) to prevent silicon sulfide formation during the reaction with  $\text{H}_2\text{S}$  [66]. The passivated windows were then coated with  $\text{WO}_3$  using atomic layer deposition in an oxygen plasma [39]. The thickness of  $\text{WO}_3$  was calculated from the required thickness of  $\text{WS}_2$  using the ratio of the density between the two assuming no W loss in the reaction with  $\text{H}_2\text{S}$ . The thickness of the oxide film was characterized by *in situ* spectroscopic ellipsometry. After the oxide deposition, the windows were put in a quartz boat and transferred into a tube furnace which was heated up to 600 °C.  $\text{H}_2\text{S}$  [5 cm<sup>3</sup>/min at STP (sccm)] and Ar (100 sccm) as a buffer gas was flowed into the tube to react with  $\text{WO}_3$ . After 1 h of reaction, the  $\text{H}_2\text{S}$  flow was turned off while maintaining the Ar flow to prevent contamination from outside air, and the furnace was left to cool down. After the temperature decreased below 200 °C, the Ar flow was switched to  $\text{N}_2$ , and the samples were taken out after the instrument reached room temperature. To verify that the absorption peaks below 37 eV are not due to defect-induced color centers, the XUV absorption spectrum of the synthesized film was compared with the total electron yield (TEY) spectrum of single-crystal  $\text{WS}_2$  (2Dsemiconduc-

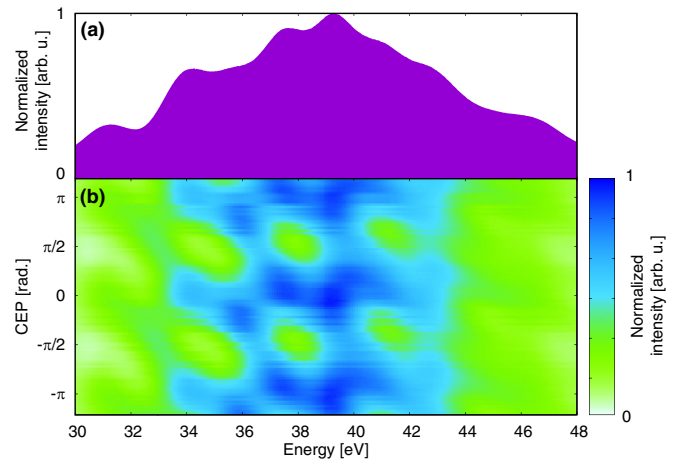


FIG. 8. (a) A typical XUV spectrum produced by high-harmonic generation in Kr and (b) the XUV spectra as a function of the carrier envelope phase of the driving pulse.

tors USA) measured at Beamline 4.0.3 at the Advanced Light Source (Appendix F).

#### APPENDIX B: EXPERIMENTAL SETUP

The optical and XUV pulses in the experiment were produced by a Ti:sapphire carrier envelope phase (CEP) stabilized laser operating at 1 kHz (Femtopower Compact Pro seeded by Femtolaser Rainbow CEP3). The output of the Ti:sapphire laser was 1.8 mJ in pulse energy and approximately 30 fs in pulse duration. The laser beam was focused into a 1-m-long Ne-filled hollow core fiber to generate a supercontinuum spanning 500–1000 nm wavelength with self-phase modulation. A mechanical chopper was installed after the hollow core fiber to chop down the repetition rate to 100 Hz to prevent sample damage through excessive heating. The dispersion accumulated during pulse propagation was compensated by a set of broadband double-angle chirped mirrors (PC70, UltraFast Innovations) and a 2-mm-thick ammonium diphosphate crystal [67]. The beam was then separated into the probe and pump arm by a 9:1 broadband beamsplitter. Each arm was equipped with a pair of UV-graded fused silica wedges for dispersion fine-tuning. The probe beam was subsequently focused into a Kr gas jet to produce broadband XUV pulses (30–50 eV) via high-harmonic generation (Fig. 8). The XUV beam then traveled through a 100-nm-thick Al filter blocking the high-harmonic driving field and was focused onto the sample with a Au-coated toroidal mirror. The pump beam was time delayed with respect to the probe by a piezo-driven optical delay stage and was subsequently recombined with the probe arm by an annular mirror. A 200-nm-thick Al filter is placed after the sample to prevent the pump beam reaching the XUV spectrometer. The XUV beam passing through the sample and the Al filter was dispersed by a flat-field grating onto an XUV CCD camera. The spectral energies were calibrated with the autoionization lines of Ar  $3s3p^6np$  and Ne  $2s2p^6np$  states [68,69]. The duration of the pump pulse was characterized by dispersion scan [70] to be  $\tau_{\text{pump}} = 4.2 \pm 0.1$  fs, and the spectrum and temporal profile of the pump pulse are shown

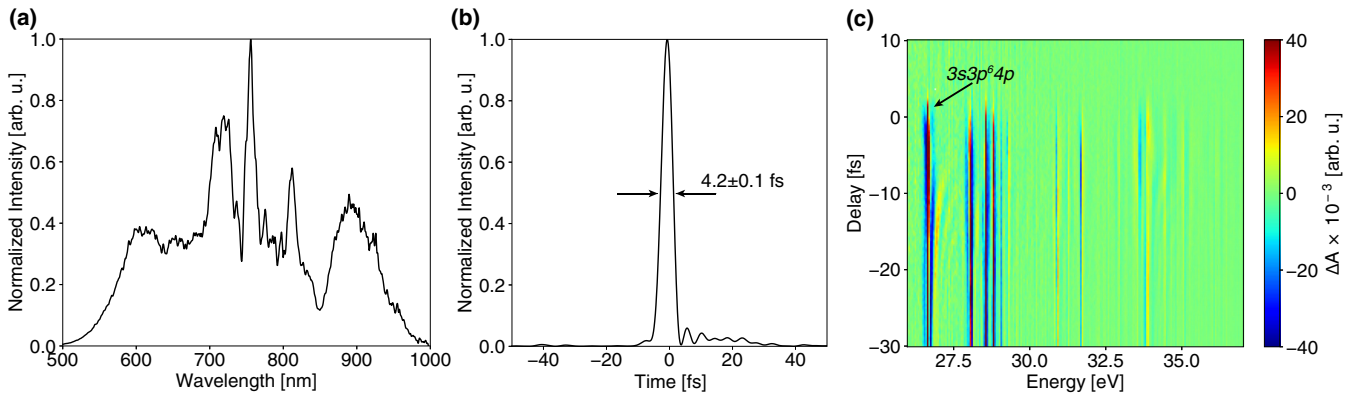


FIG. 9. (a) Intensity-calibrated spectrum and (b) temporal profile of the pump pulse. (c) Transient absorption spectra of Ar  $3s3p^6np$  autoionization states for time-zero calibration.

in Figs. 9(a) and 9(b), respectively. The pulse energy of the pump beam was controlled by an iris, and the beam profile of the pump pulses was imaged directly at the sample position with a complementary metal-oxide semiconductor (CMOS) camera to calculate the pump fluence. During the XUV transient absorption experiment, the sample was raster scanned to prevent heat damage.

To correct for the drift of time delay during the experiments, an optical-XUV transient absorption measurement on Ar was conducted after each WS<sub>2</sub> transient absorption scan [4,7]. The Ar gas cell was mounted alongside the WS<sub>2</sub> sample. The suppression of Ar  $3s3p^6np$  autoionization lines by the optical pulse at 26–37 eV photon energies was measured [Fig. 9(c)] [53,69], and the time reference of each scan was determined by fitting the integrated absolute value of the transient absorption signal of the Ar  $3s3p^64p$  state along the energy axis and fitting it with a Gaussian error function [4]. The time axis of each WS<sub>2</sub> transient absorption scan was shifted according to its time-zero reference and the transient absorption signal  $\Delta A$  interpolated onto a uniform time delay grid. In addition to time-zero referencing, the cross-correlation time between the pump and probe pulses was estimated by the width of the error function rise [4,53], and the estimated pump-probe cross-correlation time is  $\tau_{cc} = 4.1 \pm 0.5$  fs. The maximal cross-correlation time of the 4.2 fs pump pulse and a single-cycle driving pulse for high-harmonic generation centered at 730 nm [Fig. 9(a)] is  $\sqrt{4.2^2 + 2.4^2} \approx 4.8$  fs. The experimentally measured cross-correlation time of  $4.1 \pm 0.5$  fs is within the cross correlation

of the pump pulse and a single-cycle driving pulse, and the maximum width of the XUV pulse train envelope is estimated to be  $\sqrt{(\max \tau_{cc})^2 - (\min \tau_{\text{pump}})^2} \approx 2.1$  fs, less than two half cycles of the optical driving field. This indicates that the attosecond XUV pulse train consists of  $\leq 2$  XUV bursts.

To provide a reference for future studies on carrier effects on core excitons in solids that cannot be prepared as thin films, we performed XUV transient reflectivity experiments on 40-nm-thick WS<sub>2</sub> thin films deposited on silicon wafers, which were synthesized alongside the samples for XUV transient absorption experiments (Appendix A). The measurements were taken on a beamline almost identical to the one for XUV transient absorption, except for the interaction geometry at the sample [71]. The optical pump and XUV probe pulses ( $p$  and  $s$  polarized, respectively) impinged on the sample surface with a  $66^\circ$  angle from the sample normal. The reflected XUV beam was directed into a spectrometer identical to the one used in absorption. A gold mirror was used as a reference to extract the absolute reflectivity of the WS<sub>2</sub> sample [71], and because of the relatively weak change in reflectivity, the data were processed using edge-pixel referencing [72]. The results of the XUV reflectivity measurements are detailed in Appendix G.

### APPENDIX C: ELECTRONIC STRUCTURE CALCULATIONS

The electronic structure of bulk WS<sub>2</sub> is computed with the all-electron full-potential linearized augmented plane wave (FP-LAPW) method using the ELK code [41,73]. The

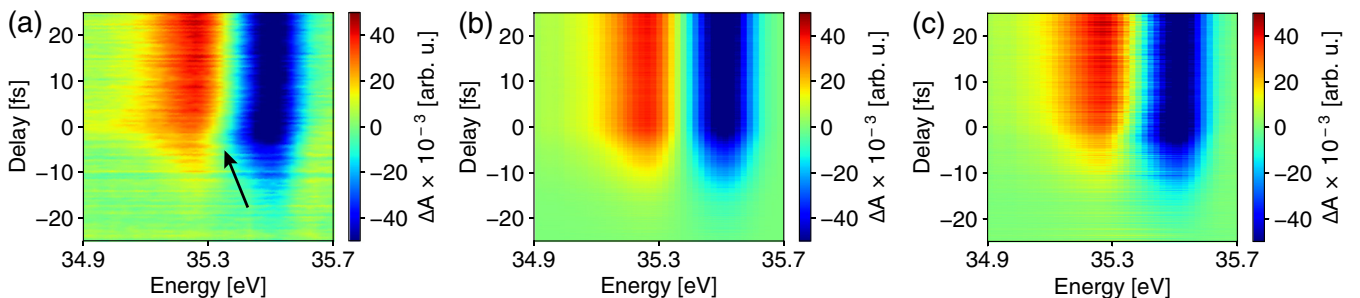


FIG. 10. (a) Experimental short-time XUV TA spectra at transition C. (b) shows the reconstruction of the XUV spectra with the first (largest) spectral component, and (c) shows the reconstruction with the first and second components.

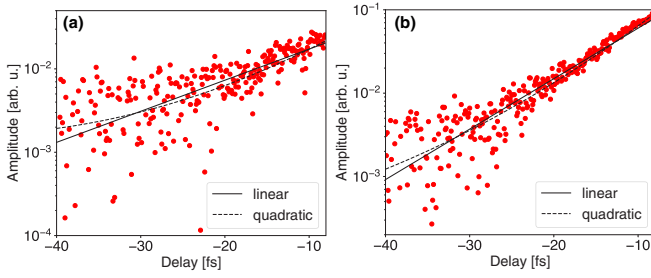


FIG. 11. Quadratic fitting (dashed line) of the logarithm of the largest component in the SVD of the XUV TA signal at (a) core-exciton transitions A and B and (b) core-exciton transition C. The data points from the SVD are shown as red dots. Results of linear fitting of the components are shown as black solid lines.

density functional theory (DFT) computation is conducted within the local spin density approximation (LSDA) [74]. Spin-orbit coupling effects are included, and the calculations are converged with a  $k$  grid of  $10 \times 10 \times 3$   $k$  points. A 4 eV blueshift is added to the calculated dielectric function in Fig. 1(a) to compensate the underestimated gap between the core levels and the CB in DFT calculations.

The number of photons available in the optical pulse to excite valence electron-hole pairs as a function of  $k$  points (Fig. 4) is calculated with the formula

$$N_{\text{ph,exc}}(\mathbf{k}) = \sum_{n_v, n_c} \int dE N_{\text{ph}}(E) \delta[E_{n_c}(\mathbf{k}) - E_{n_v}(\mathbf{k})].$$

The number of photons as a function of photon energy  $N_{\text{ph}}(E)$  is obtained from the measured spectrum of the pump pulse [Fig. 9(a)]. The energies of valence and conduction bands  $n_v$  and  $n_c$  are obtained from the calculated band structure [Fig. 4(b)].

#### APPENDIX D: OPTICALLY EXCITED CARRIER DENSITY

The photoexcited carrier density  $\rho_{\text{exc}}$  is estimated by calculating the number of absorbed photons in the 40-nm-thick  $\text{WS}_2$  film per unit area  $\sigma_{\text{abs}}$  divided by the thickness of the film  $d$ :  $\rho_{\text{exc}} = \sigma_{\text{abs}}/d$ . The number of photons absorbed per unit area can be calculated with the equation

$$\sigma_{\text{abs}} = \int d\omega \bar{\sigma}_{\text{inc}}(\omega) f_{\text{abs}}(\omega),$$

where  $\bar{\sigma}_{\text{inc}}(\omega)$  is the number of incident photons per unit area with photon energy  $\omega$  and  $f_{\text{abs}}$  is the fraction of photons absorbed in the film.  $\bar{\sigma}_{\text{inc}}(\omega)$  can be calculated from the spectrum of the pump pulse and the measured fluence. The fraction of photons absorbed ( $f_{\text{abs}}$ ) is calculated using the transfer matrix method including the 40-nm-thick  $\text{WS}_2$  film and the silicon nitride window [75]. The refractive indices of  $\text{WS}_2$  and silicon nitride are taken from Refs. [76,77]. We conducted the experiments with fluences ranging from 6 to 30  $\text{mJ}/\text{cm}^2$ , and the resulting calculated excited carrier density ranges from  $3 \times 10^{20}$  to  $2 \times 10^{21} \text{ cm}^{-3}$ . The carrier density per layer is calculated multiplying the carrier density by volume with the layer thickness of 6.2 Å [78].

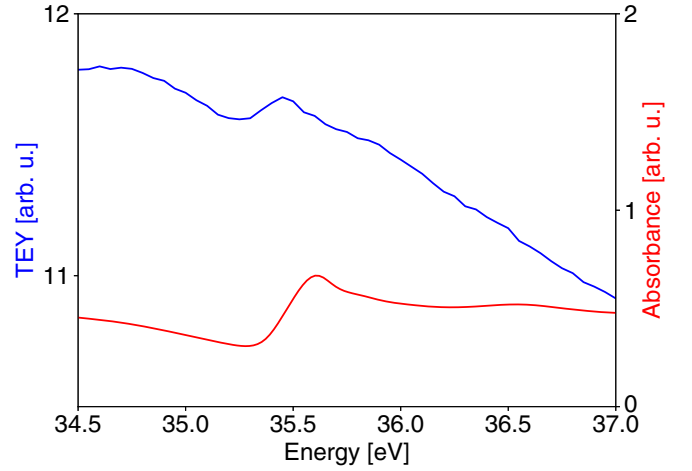


FIG. 12. Normalized total electron yield spectrum of single-crystal  $\text{WS}_2$  measured at Beamline 4.0.3 at the Advanced Light Source (blue) and the XUV absorption spectrum of 40-nm-thick  $\text{WS}_2$  thin film used in the core-level transient absorption experiment (red).

#### APPENDIX E: SINGULAR VALUE DECOMPOSITION

The XUV TA spectra between  $-25$  and  $25$  fs below 37.5 eV are analyzed with global fitting via singular value decomposition (SVD), where the TA signal  $\Delta A(t, E)$  is written as a matrix with rows and columns indicating different time  $t$  and energy  $E$ , respectively (Figs. 5 and 10). The TA matrix  $\Delta A(t, E)$  is then decomposed with SVD into  $\Delta A(t, E) = U(t)^T S V(E)$ , where  $U$  and  $V$  are unitary matrices consisting of singular vectors  $\{u_n(t)\}$  and  $\{v_n(E)\}$ , respectively.  $S$  is a rectangular diagonal matrix, and the diagonal matrix elements  $S_{nn} = s_n$  are singular values ranked in descending order. The reconstruction of the TA signal  $\Delta A_{\text{rec}}(t, E)$  by components up to the  $n$ th rank is defined as  $\Delta A_{\text{rec}}(t, E) = \sum_{m=1}^n s_m u_m(t) v_m(E)$ . Note that the SVD approach is based on the assumption that the transient absorption spectra can be represented by a linear combination of components from different contributions. Here, such an assumption is valid because the carrier-induced spectral modification is the dominant contributor [Figs. 5(a)–5(c)] and the direct field-induced effects can be regarded as a minor component.

To verify whether phonon-induced dephasing contributes significantly to the decay of core excitons, we focus on the decay dynamics of the largest component in the SVD,  $u_1(t)$  [Figs. 5(c) and 5(f), red dots], at negative delays. The largest SVD component is plotted in logarithmic scale in Fig. 11, and the component  $\log_{10} u_1(t)$  is fitted with a quadratic function  $at^2 + bt + c$ . The fitted coefficients of the quadratic function

TABLE I. Results of quadratic fitting of  $\log_{10} u_1(t)$  for core excitons A and B and core exciton C (Fig. 11).

	A and B	C
$a$	$(6 \pm 2) \times 10^{-4}$	$(5 \pm 2) \times 10^{-4}$
$b$	$0.061 \pm 0.008$	$0.084 \pm 0.007$
$c$	$-1.21 \pm 0.06$	$-0.4 \pm 0.07$

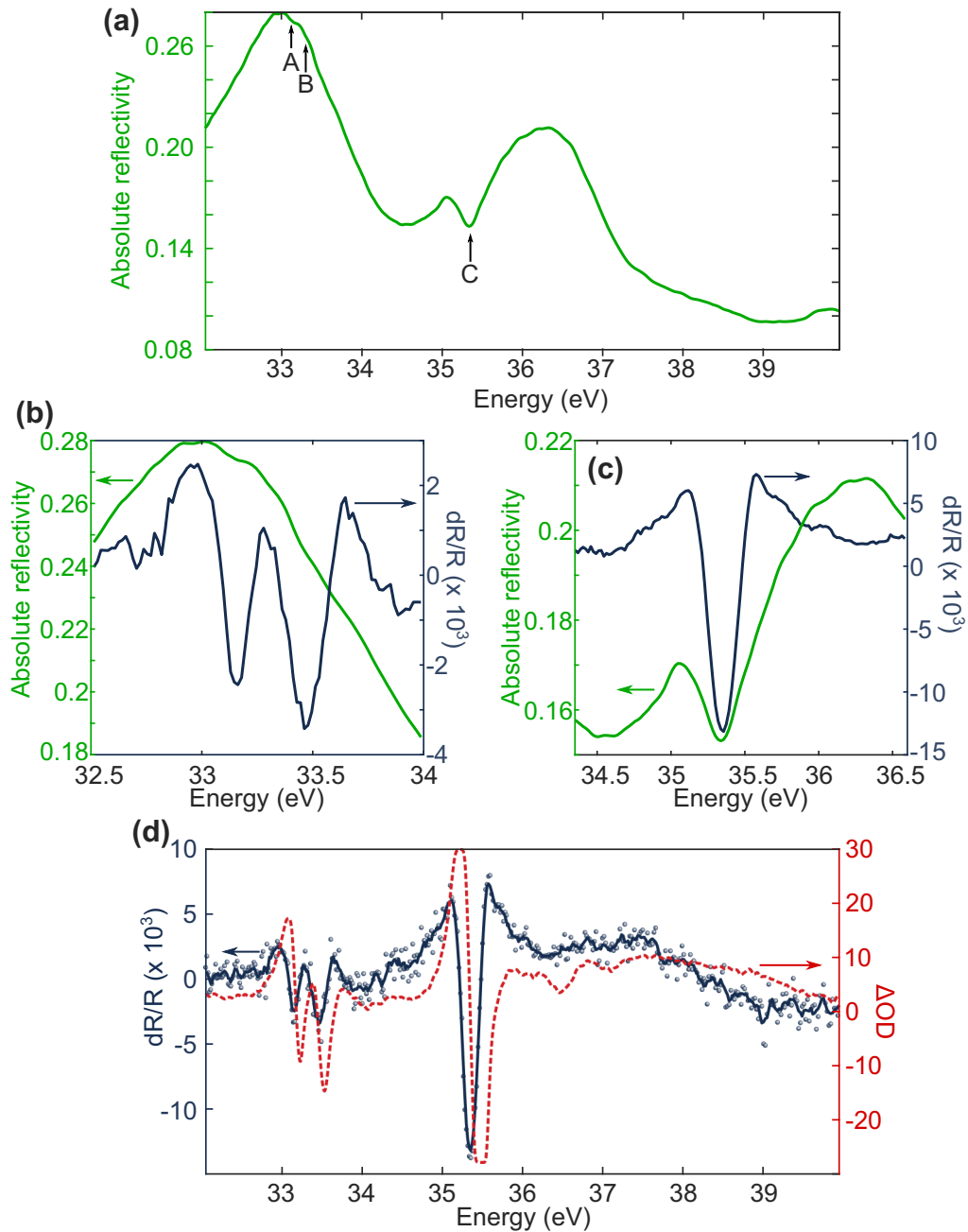


FIG. 13. (a) Static XUV reflectivity (*s* polarized) of WS<sub>2</sub>. The core-exciton transitions A, B, and C are labeled. (b) and (c) present the transient reflectivity  $dR/R = (R_{\text{on}} - R_{\text{off}})/R_{\text{off}}$  of core-excitations A, B, and C at +10 fs delay. (d) displays the changes in reflectivity at +10 fs (blue points), together with a five-point moving average (blue solid line), overlaid with the changes in optical density at the same pump-probe delay (red dashed line). The pump fluence used to obtain the transient reflectivity results is 25 mJ/cm<sup>2</sup>. The reflectivity with and without the optical pump is denoted as  $R_{\text{on}}$  and  $R_{\text{off}}$ , respectively.

are listed in Table I, showing that the quadratic term  $a$  is two orders of magnitude smaller than the linear term  $b$ . In addition, the fitted  $a$  are positive rather than negative as expected for a Gaussian function. This indicates that the decay of XUV TA signal at negative time delays is exponential rather than Gaussian and the effect of phonon-induced dephasing is insignificant.

#### APPENDIX F: COMPARISON WITH XUV TOTAL ELECTRON YIELD OF SINGLE-CRYSTAL WS<sub>2</sub>

To verify that the absorption peaks below 37 eV are not due to defect-induced color centers, the XUV absorption spectrum of the synthesized film is compared with the total electron yield (TEY) spectrum of single-crystal WS<sub>2</sub> (2Dsemiconductors USA) measured at Beamline 4.0.3 at the Advanced Light

Source. The measured TEY of the single-crystal sample is shown in Fig. 12. The spectrum is cut off at 34.5 eV due to the lack of XUV photons below 34.5 eV at the undulator beamline. The measured TEY of WS<sub>2</sub> shown in Fig. 12 is normalized by the measured TEY of a gold film:  $TEY_{\text{norm}} = TEY_{\text{sample}}/TEY_{\text{Au}}$ .

#### APPENDIX G: ADDITIONAL STATIC AND TRANSIENT REFLECTIVITY MEASUREMENTS

Here, we provide measurements of core-exciton dynamics in the presence of photoexcited carriers in reflectivity geometry. Certain materials are challenging to synthesize as thin films for XUV absorption measurements; yet the analysis of reflectivity data alone is challenging and often relies on

Kramers-Kronig transforms. Therefore the data presented below can serve as a useful reference point for future studies of materials other than WS<sub>2</sub>.

The absolute static reflectivity of WS<sub>2</sub> deposited on a silicon wafer, taken at 66° from normal [Fig. 13(a)], shows that while core exciton C is very visible, core excitons A and B are difficult to resolve. Nevertheless, reflectivity changes are clearly observed [shown in Figs. 13(b) and 13(c) at +10 fs delay] for each peak and share the same shape: a reduced reflectivity at the center of the exciton lineshape and a slight increase on each side of it. The comparison [Fig. 13(d)] with the transient absorption reported in the main text shows that the two observables are consistent with each other. These results display how the core-excitonic lineshapes in reflection geometry are modified by the excitation of free carriers.

- [1] J. Shah, *Ultrafast Spectroscopy of Semiconductors and Semiconductor Nanostructures*, Springer Series in Solid-State Sciences Vol. 115 (Springer, New York, 1996).
- [2] S. W. Koch, M. Kira, G. Khitrova, and H. M. Gibbs, *Nat. Mater.* **5**, 523 (2006).
- [3] M. Schultze, K. Ramasesha, C. D. Pemmaraju, S. A. Sato, D. Whitmore, A. Gandman, J. S. Prell, L. J. Borja, D. Prendergast, K. Yabana, D. M. Neumark, and S. R. Leone, *Science* **346**, 1348 (2014).
- [4] M. Zürich, H.-T. Chang, L. J. Borja, P. M. Kraus, S. K. Cushing, A. Gandman, C. J. Kaplan, M. H. Oh, J. S. Prell, D. Prendergast, C. D. Pemmaraju, D. M. Neumark, and S. R. Leone, *Nat. Commun.* **8**, 15734 (2017).
- [5] M. F. Lin, M. A. Verkamp, J. Leveillee, E. S. Ryland, K. Benke, K. Zhang, C. Weninger, X. Shen, R. Li, D. Fritz, U. Bergmann, X. Wang, A. Schleife, and J. Vura-Weis, *J. Phys. Chem. C* **121**, 27886 (2017).
- [6] M. A. Verkamp, J. Leveillee, A. Sharma, A. Schleife, and J. Vura-Weis, *ChemRxiv*, 10.26434/chemrxiv.8323289.v1.
- [7] A. R. Attar, H.-T. Chang, A. Britz, X. Zhang, M.-F. Lin, A. Krishnamoorthy, T. Linker, D. Fritz, D. M. Neumark, R. K. Kalia, A. Nakano, P. Ajayan, P. Vashishta, U. Bergmann, and S. R. Leone, *ACS Nano* **14**, 15829 (2020).
- [8] F. Schlaepfer, M. Lucchini, S. A. Sato, M. Volkov, L. Kasmi, N. Hartmann, A. Rubio, L. Gallmann, and U. Keller, *Nat. Phys.* **14**, 560 (2018).
- [9] B. Buades, A. Picon, E. Berger, I. Leon, N. Di Palo, S. L. Cousin, C. Cocchi, E. Pellegrin, J. H. Martin, S. Mañas-Valero, E. Coronado, T. Danz, C. Draxl, M. Uemoto, K. Yabana, M. Schultze, S. Wall, M. Zürich, and J. Biegert, *arXiv:1808.06493*.
- [10] A. Britz, A. R. Attar, X. Zhang, H.-T. Chang, C. Nyby, A. Krishnamoorthy, S. H. Park, S. Kwon, M. Kim, D. Nordlund, S. Sainio, T. F. Heinz, S. R. Leone, A. M. Lindenberg, A. Nakano, P. Ajayan, P. Vashishta, D. Fritz, M.-F. Lin, and U. Bergmann, *Struct. Dyn.* **8**, 014501 (2021).
- [11] A. Moulet, J. B. Bertrand, T. Klostermann, A. Guggenmos, N. Karpowicz, and E. Goulielmakis, *Science* **357**, 1134 (2017).
- [12] R. Généaux, C. J. Kaplan, L. Yue, A. D. Ross, J. E. Bækhoj, P. M. Kraus, H.-T. Chang, A. Guggenmos, M.-Y. Huang, M. Zürich, K. J. Schafer, D. M. Neumark, M. B. Gaarde, and S. R. Leone, *Phys. Rev. Lett.* **124**, 207401 (2020).
- [13] M. Lucchini, S. A. Sato, G. D. Lucarelli, B. Moio, G. Inzani, R. Borrego-Varillas, F. Frassetto, L. Poletto, H. Hübener, U. De Giovannini, A. Rubio, and M. Nisoli, *Nat. Commun.* **12**, 1021 (2020).
- [14] J. J. Rehr, *Found. Phys.* **33**, 1735 (2003).
- [15] For literature of core excitons in insulators, see A. Balzarotti and M. Piacentini, in *Electronic Structure and Electronic Transitions in Layered Materials*, edited by V. Grasso (Springer, Dordrecht, 1986), pp. 289–398, and references therein.
- [16] F. Bassani, *Appl. Opt.* **19**, 4093 (1980).
- [17] H. P. Hjalmarson, H. Büttner, and J. D. Dow, *Phys. Rev. B* **24**, 6010 (1981).
- [18] G. Strinati, *Phys. Rev. Lett.* **49**, 1519 (1982).
- [19] F. de Groot and A. Kotani, *Core Level Spectroscopy of Solids*, Advances in Condensed Matter Science Vol. 6 (CRC Press, Boca Raton, 2008).
- [20] M. Zürich, H.-T. Chang, P. M. Kraus, S. K. Cushing, L. J. Borja, A. Gandman, C. J. Kaplan, M. H. Oh, J. S. Prell, D. Prendergast, C. D. Pemmaraju, D. M. Neumark, and S. R. Leone, *Struct. Dyn.* **4**, 044029 (2017).
- [21] A. R. Beck, D. M. Neumark, and S. R. Leone, *Chem. Phys. Lett.* **624**, 119 (2015).
- [22] H. Jiang, *J. Phys. Chem. C* **116**, 7664 (2012).
- [23] A. Berkdemir, H. R. Gutiérrez, A. R. Botello-Méndez, N. Perea-López, A. L. Elías, C.-I. Chia, B. Wang, V. H. Crespi, F. López-Urías, J.-C. Charlier, H. Terrones, and M. Terrones, *Sci. Rep.* **3**, 1755 (2013).
- [24] H. R. Gutiérrez, N. Perea-López, A. L. Elías, A. Berkdemir, B. Wang, R. Lv, F. López-Urías, V. H. Crespi, H. Terrones, and M. Terrones, *Nano Lett.* **13**, 3447 (2013).
- [25] A. Chernikov, T. C. Berkelbach, H. M. Hill, A. Rigosi, Y. Li, O. B. Aslan, D. R. Reichman, M. S. Hybertsen, and T. F. Heinz, *Phys. Rev. Lett.* **113**, 076802 (2014).
- [26] Z. Ye, T. Cao, K. O'Brien, H. Zhu, X. Yin, Y. Wang, S. G. Louie, and X. Zhang, *Nature (London)* **513**, 214 (2014).
- [27] E. J. Sie, J. W. McIver, Y.-H. Lee, L. Fu, J. Kong, and N. Gedik, *Nat. Mater.* **14**, 290 (2014).
- [28] A. Chernikov, C. Ruppert, H. M. Hill, A. F. Rigosi, and T. F. Heinz, *Nat. Photon.* **9**, 466 (2015).
- [29] A. Chernikov, A. M. van der Zande, H. M. Hill, A. F. Rigosi, A. Velauthapillai, J. Hone, and T. F. Heinz, *Phys. Rev. Lett.* **115**, 126802 (2015).
- [30] A. Raja, A. Chaves, J. Yu, G. Arefe, H. M. Hill, A. F. Rigosi, T. C. Berkelbach, P. Nagler, C. Schüller, T. Korn, C. Nuckolls, J. Hone, L. E. Brus, T. F. Heinz, D. R.

- Reichman, and A. Chernikov, *Nat. Commun.* **8**, 15251 (2017).
- [31] P. Nagler, M. V. Ballottin, A. A. Mitioglu, M. V. Durnev, T. Taniguchi, K. Watanabe, A. Chernikov, C. Schüller, M. M. Glazov, P. C. M. Christianen, and T. Korn, *Phys. Rev. Lett.* **121**, 057402 (2018).
- [32] A. Raja, M. Selig, G. Berghäuser, J. Yu, H. M. Hill, A. F. Rigosi, L. E. Brus, A. Knorr, T. F. Heinz, E. Malic, and A. Chernikov, *Nano Lett.* **18**, 6135 (2018).
- [33] H. Su, A. Deng, Z. Zhen, and J.-F. Dai, *Phys. Rev. B* **97**, 115426 (2018).
- [34] J. Gu, B. Chakraborty, M. Khatoniar, and V. M. Menon, *Nat. Nanotechnol.* **14**, 1024 (2019).
- [35] C. Jin, J. Kim, M. Iqbal Bakti Utama, E. C. Regan, H. Kleemann, H. Cai, Y. Shen, M. J. Shinner, A. Sengupta, K. Watanabe, T. Taniguchi, S. Tongay, A. Zettl, and F. Wang, *Science* **360**, 893 (2018).
- [36] L. Yuan, T.-F. Chung, A. Kuc, Y. Wan, Y. Xu, Y. P. Chen, T. Heine, and L. Huang, *Sci. Adv.* **4**, e1700324 (2018).
- [37] C. Jin, E. C. Regan, A. Yan, M. Iqbal Bakti Utama, D. Wang, S. Zhao, Y. Qin, S. Yang, Z. Zheng, S. Shi, K. Watanabe, T. Taniguchi, S. Tongay, A. Zettl, and F. Wang, *Nature (London)* **567**, 76 (2019).
- [38] H. Li, S. Li, M. H. Naik, J. Xie, X. Li, J. Wang, E. Regan, D. Wang, W. Zhao, S. Zhao, S. Kahn, K. Yumigeta, M. Blei, T. Taniguchi, K. Watanabe, S. Tongay, A. Zettl, S. G. Louie, F. Wang, and M. F. Crommie, *Nat. Mater.* **20**, 945 (2021).
- [39] C. Kastl, C. T. Chen, T. Kuykendall, B. Shevitski, T. P. Darlington, N. J. Borys, A. Krayev, P. J. Schuck, S. Aloni, and A. M. Schwartzberg, *2D Mater.* **4**, 021024 (2017).
- [40] U. Fano, *Phys. Rev.* **124**, 1866 (1961).
- [41] The Elk code, <http://elk.sourceforge.net/>.
- [42] G. Onida, L. Reining, and A. Rubio, *Rev. Mod. Phys.* **74**, 601 (2002).
- [43] S.-i. Nakai and T. Sagawa, *J. Phys. Soc. Jpn.* **26**, 1427 (1969).
- [44] W. L. O'Brien, J. Jia, Q.-Y. Dong, T. A. Callcott, J.-E. Rubensson, D. L. Mueller, and D. L. Ederer, *Phys. Rev. B* **44**, 1013 (1991).
- [45] P. B. Allen and M. Cardona, *Phys. Rev. B* **27**, 4760 (1983).
- [46] S. K. Cushing, M. Zürich, P. M. Kraus, L. M. Carneiro, A. Lee, H.-T. Chang, C. J. Kaplan, and S. R. Leone, *Struct. Dyn.* **5**, 054302 (2018).
- [47] S. K. Cushing, A. Lee, I. J. Porter, L. M. Carneiro, H.-T. Chang, M. Zürich, and S. R. Leone, *J. Phys. Chem. C* **123**, 3343 (2019).
- [48] Y. H. Lee, A. Chavez-Pirson, S. W. Koch, H. M. Gibbs, S. H. Park, J. Morhange, A. Jeffery, N. Peyghambarian, L. Banyai, A. C. Gossard, and W. Wiegmann, *Phys. Rev. Lett.* **57**, 2446 (1986).
- [49] H. Haug and S. Schmitt-Rink, *Prog. Quantum Electron.* **9**, 3 (1984).
- [50] Y. Li, W. Liu, Y. Wang, Z. Xue, Y.-C. Leng, A. Hu, H. Yang, P.-H. Tan, Y. Liu, H. Misawa, Q. Sun, Y. Gao, X. Hu, and Q. Gong, *Nano Lett.* **20**, 3747 (2020).
- [51] Z. Nie, R. Long, L. Sun, C.-C. Huang, J. Zhang, Q. Xiong, D. W. Hewak, Z. Shen, O. V. Prezhdo, and Z.-H. Loh, *ACS Nano* **8**, 10931 (2014).
- [52] L. Waldecker, R. Bertoni, H. Hübener, T. Brumme, T. Vasileiadis, D. Zahn, A. Rubio, and R. Ernstorfer, *Phys. Rev. Lett.* **119**, 036803 (2017).
- [53] H. Wang, M. Chini, S. Chen, C.-H. Zhang, F. He, Y. Cheng, Y. Wu, U. Thumm, and Z. Chang, *Phys. Rev. Lett.* **105**, 143002 (2010).
- [54] C. Ott, A. Kaldun, P. Raith, K. Meyer, M. Laux, J. Evers, C. H. Keitel, C. H. Greene, and T. Pfeifer, *Science* **340**, 716 (2013).
- [55] A. Kaldun, C. Ott, A. Blättermann, M. Laux, K. Meyer, T. Ding, A. Fischer, and T. Pfeifer, *Phys. Rev. Lett.* **112**, 103001 (2014).
- [56] T. Ding, C. Ott, A. Kaldun, A. Blättermann, K. Meyer, V. Stooss, M. Rebholz, P. Birk, M. Hartmann, A. Brown, H. V. D. Hart, and T. Pfeifer, *Opt. Lett.* **41**, 709 (2016).
- [57] K. Huang and A. Rhys, *Proc. R. Soc. Lond. A* **204**, 406 (1950).
- [58] P. H. Citrin, P. Eisenberger, and D. R. Hamann, *Phys. Rev. Lett.* **33**, 965 (1974).
- [59] As an additional note, while the lifetimes of the core excitons can be potentially extracted from the core-exciton linewidth in the XUV static absorption spectrum, the overlap between the discrete core-exciton transitions and the continuous core-to-CB transitions [Fig. 1(a)] makes the linewidth extraction unreliable.
- [60] R. J. Elliott, *Phys. Rev.* **108**, 1384 (1957).
- [61] L. Bányai and S. W. Koch, *Z. Phys. B: Condens. Matter* **63**, 283 (1986).
- [62] S. W. Koch, N. Peyghambarian, and H. M. Gibbs, *J. Appl. Phys. (Melville, NY)* **63**, R1 (1988).
- [63] H. Haug and D. B. T. Thoai, *Phys. Status Solidi B* **85**, 561 (1978).
- [64] R. Zimmermann, K. Kilimann, W. D. Kraeft, D. Kremp, and G. Röpke, *Phys. Status Solidi B* **90**, 175 (1978).
- [65] S. Schmitt-Rink, C. Ell, and H. Haug, *Phys. Rev. B* **33**, 1183 (1986).
- [66] *Handbook of Semiconductor Manufacturing Technology*, 2nd ed., edited by R. Doering and Y. Nishi (CRC Press, Boca Raton, 2008).
- [67] H. Timmers, Y. Kobayashi, K. F. Chang, M. Reduzzi, D. M. Neumark, and S. R. Leone, *Opt. Lett.* **42**, 811 (2017).
- [68] K. Codling, R. P. Madden, and D. L. Ederer, *Phys. Rev.* **155**, 26 (1967).
- [69] R. P. Madden, D. L. Ederer, and K. Codling, *Phys. Rev.* **177**, 136 (1969).
- [70] F. Silva, M. Miranda, B. Alonso, J. Rauschenberger, V. Pervak, and H. Crespo, *Opt. Express* **22**, 10181 (2014).
- [71] C. J. Kaplan, P. M. Kraus, A. D. Ross, M. Zürich, S. K. Cushing, M. F. Jager, H.-T. Chang, E. M. Gullikson, D. M. Neumark, and S. R. Leone, *Phys. Rev. B* **97**, 205202 (2018).
- [72] R. Géneaux, H.-T. Chang, A. M. Schwartzberg, and H. J. B. Marroux, *Opt. Express* **29**, 951 (2021).
- [73] D. J. Singh and L. Nordström, *Planewaves, Pseudopotentials, and the LAPW Method*, 2nd ed. (Springer, New York, 2006).
- [74] J. P. Perdew and Y. Wang, *Phys. Rev. B* **45**, 13244 (1992).
- [75] G. F. Burkhard, E. T. Hoke, and M. D. McGehee, *Adv. Mater. (Weinheim)* **22**, 3293 (2010).
- [76] C. Hsu, R. Frisenda, R. Schmidt, A. Arora, S. M. de Vasconcellos, R. Bratschitsch, H. S. J. van der Zant, and A. Castellanos-Gomez, *Adv. Opt. Mater.* **7**, 1900239 (2019).
- [77] M. R. Vogt, Ph.D. thesis, Gottfried Wilhelm Leibniz Universität, Hannover, 2015.
- [78] *WS<sub>2</sub> crystal structure: Datasheet from "PAULING FILE multinaries edition – 2012," in SpringerMaterials* (Springer, Berlin—Material Phases Data System, Switzerland—National Institute for Materials Science, Japan, 2012).